J. Inst. Eng. India Ser. C (October 2022) 103(5):1177–1191
https://doi.org/10.1007/s40032-022-00870-4

ORIGINAL CONTRIBUTION

Microstructural, Strength and Residual Stress Studies on Single- and Double-Side Single-Pass Submerged Arc Welding of 9Cr–1Mo–V Steel Plate

Saurav Suman[1] · **Pankaj Biswas**[2]

Received: 16 December 2021 / Accepted: 14 March 2022 / Published online: 11 August 2022

Abstract Single- and double-side single-pass square butt submerged arc welding is carried out on 9Cr–1Mo–V steel plate using the same weld materials. Deep hole drilling and contour measurement were employed to determine welding-induced residual stresses. The subsequent changes in microstructure and mechanical properties are also investigated. These weld joints are simulated and analysed considering the element birth and death, double ellipsoidal Gaussian distributed heat source model, temperature-dependent material properties, phase transformation, etc. It was observed that single-side single-pass welding develops better transverse strength properties than double-side single-pass welding. A compressive longitudinal residual stress was observed in the fusion zone throughout the thickness of the single-pass weld. However, double-sided weld exhibited tensile residual stress in the mid-thickness region of the FZ, whereas the top and bottom regions in the fusion zone of the double-sided weld possess compressive residual stress.

Keywords Submerged arc welding · Residual stress · Weld groove · FEM · 9Cr–1Mo–V steel

✉ Saurav Suman
sauravnitmz@gmail.com

[1] Department of Mechanical Engineering, National Institute of Technology, Mizoram, Chaltlang, Aizawl, Mizoram 796012, India

[2] Department of Mechanical Engineering, Indian Institute of Technology Guwahati, Kamrup, Guwahati, Assam 781039, India

Introduction

The 9Cr–1Mo–V steel or P91 steel comes under the group of creep strength enhanced ferritic (CSEF) steels. These steels possess phenomenal mechanical properties and microstructural stability in an elevated temperature (around 600 °C) working environment [1]. The high-temperature creep resistance, mechanical strength, rupture life and resistant to stress corrosion and oxidation are some key properties of this steel. Apart from those, these steels also exhibit good thermal conductivity, weldability, better ductility and toughness. Therefore, it appeared to be a superior choice for high-temperature applications such as steam pipelines, boilers, super-heaters in power plants and breeders in nuclear reactor, etc. [2]. The manufacturing processes such as welding deviate the overall properties of the steel as well as induce undesirable residual stresses and deformation. These residual stresses are found to be more deteriorating in high-temperature work pressure. On the other hand, welding-induced distortion affects the assembly of weld components to form a final structure [3]. The welding-induced stresses and distortion depend on various factors like welding methods, process parameters, welding direction and passes, material properties, shape and size of the joint, etc. The effect of heat input on residual stress has been studied for various welding processes for single- and multi-pass welding [4–8]. The increase in the amount of heat input directly increases the intensity of residual stresses especially in the fusion zone. However, it also diverges with the effect of material properties of base metal, cooling rate, etc. Kohandehghan and Serajzadeh [9] and Fu et al. [10] conducted a study on the effect of constraints in the welding experiments on residual stresses and revealed that increasing the fixture strength directly increases the intensity of residual stresses development. Welding direction and weld passes also affect the residual stress distribution. Kartal et al. conducted a

comparative study on residual stresses for one- and multi-pass manual metal arc welding of thick steel plate using neutron diffraction, contour and finite element methods. They found that three-pass weld experiences peak stress 100 MPa higher than single-pass weld [11]. Similarly, Hashemzadeh et al. [12] compared the effect of single- and multi-pass automatic gas tungsten arc welding (GTAW) on sheet for residual stress development. A symmetric distribution of residual stress was induced in one-pass welding compared to irregular pattern in multi-pass welding. However, lower peak of tensile/compressive stress was observed as expected in multi-pass welding. Mondal et al. [13] conducted comparative study of residual stress and angular deformation in single- and double-side submerged arc welded fillet joints. They discovered that single-side weld induces more and unstable residual stress distribution as compared to double-side fillet weld. Sattari-Far and Farahani conducted TIG welding on AISI 304 steel pipe with varying weld groove shapes (V, U, X in single and multi-pass) and number of welding passes (2, 4 and 6 for 6-mm-thick plate and 4, 9 and 13 for 10-mm-thick plate). The finite element modelling and deep hole drilling experiment results revealed that groove design and shape have no significant effect for thickness less than or equal to 6 mm, whereas for thickness of 10 mm, the X weld bead shape shows higher magnitude of residual stress in the mid-thickness of the pipe compared to V and U bead shape. In the similar manner, it was found that weld pass numbers do not substantially influence the residual stress distribution across the weld centreline. Still, a large number of passes increased the intensity of residual stress in the inner surface of the thin pipe, while residual stress (axial stress in inner surface of pipe and collectively in mid-thickness of pipe) evidently increased in thick plate (10 mm) weld [14]. Kannan et al. conducted single- and double-pass hybrid laser arc welding on naval grade 12-mm-thick steel for microstructure and mechanical properties [15]. Recently, few such studies were performed on P91 steel welds. Pandey et al. investigated the transverse shrinkage and residual stresses in narrow and conventional groove GTAW of P91 steel pipe. They discovered that narrow groove develops less axial and hoop stresses compared to conventional groove weld [16]. Suman et al. [17] also compared the residual stress distribution in single- and multi-pass submerged arc butt welded P91 steel plate and found that single-pass weld experiences uniform peaks in fusion zone compared to multi-pass welding.

In the present work, 10-mm-thick P91 steel plate was square butt welded with single- and double-sided single-pass submerged arc welding (SAW). The restraint, welding consumable (electrode) and flux were kept the same for both the welds. Finite element modelling with deep hole drilling and contour methods were performed to estimate the residual stress distribution. Welding-induced distortion (angular distortion and edge deflection) were also investigated for comparison. The microstructural changes and mechanical properties were deliberately considered for the effect of both the welding cases. In FE modelling, the specific possession of solid-state phase transformation in P91 steel weld was successfully implemented along with the effect of transformation plasticity and temperature-dependent material properties. Element birth and death technique were applied to simulate the real-time addition of molten metal throughout the welding. It was found that different amount of heat input in single- and double-side welding affects the heat-affected zone (HAZ) width, microstructure and as a result mechanical property of the weld. The mid-thickness of the plate displays tensile residual stress in double-sided weld compared to compressive longitudinal residual stress for single-sided weld. However, the top and bottom fusion regions possess compressive longitudinal residual stress for both single- and double-side welded joints.

Experimental Procedures

Materials and Weld Preparation

ASTM A 387 Grade 91 steel plate with chemical compositions given in Table 1 was selected as 9Cr–1Mo–V steel base plate to make single-side single-pass and double-side single-pass square butt weld joints. The dimension of each plate of the square butt joint is $150 \times 75 \times 10$ mm^3. The electrode wire with manufacturer code OK AUTROD 13.20 (EB-3-21/4Cr1Mo) and electrode classification as AWS A5.23 wire: EB3R was used as the consumable for all the welds. A basic flux with manufacturer code OK FLUX 10.62 of grain size (0.2–1.6 mm) suggested for the selected electrode was used throughout the submerged arc welding of both the cases [18, 19, 20]. The base plates were tack welded at both the ends with manual metal arc welding right before the actual welding starts. The root gap for both the welds was taken 2.5 mm for square butt welding [18, 21]. A specially designed aluminium backing plate (prefilled with flux bed over it) was engaged to achieve good bottom reinforcement in single-side welding. The welding parameters for both the weld joints are given in Table 2.

Table 1 Compositions of base metal and electrode wire

Elements	Si	C	P	Mn	S	Cr	V	Mo	N	Cu	Ni
Base metal (wt%)	0.29	0.1	0.016	0.46	0.001	8.69	0.22	0.89	0.039	–	0.27
Electrode wire (wt%)	0.16	0.11	0.008	0.7	0.002	4.28	0.01	0.9	0.0067	0.07	0.05

As far as amount of heat input is concerned, the total net heat input in each pass of welding can be calculated using Eq. (1) [22], where HI represents the total heat input, V and I are the welding voltage and current and v is the welding torch speed in mm/sec. Single-side single-pass welding observed the heat input of 2.3 kJ/mm, whereas in double-side welding, the heat input in first pass and second pass was around 1.8 kJ/mm and 1.9 kJ/mm, respectively.

$$\mathrm{HI} = \frac{\eta \times V \times I}{v \times 1000}\ (\mathrm{kJ/mm}) \tag{1}$$

The K-type thermocouple was attached at different locations on top and bottom surfaces of the weld plates away from the weld centreline to record the temperature profile during the welding. The recorded temperature profile helped in efficient FE modelling of the welding process.

Residual Stress Measurement

Deep hole drilling (DHD) and contour techniques were employed to measure the residual stress distribution in single- and double-side welded joints, respectively. Both the techniques work on the principle of relaxation of trapped stress distribution across the weld under corresponding deformation involved in the experiments. DHD technique estimates biaxial residual stress distribution at a point in longitudinal and transverse directions, whereas in contour technique the residual stress is determined in the perpendicular direction of the contour surface after cut. In DHD measurement, the whole experiments were accomplished in 4 major steps as explained in schematic shown in Fig. 1. A hole is drilled across the thickness of the weld plate in the targeted region, i.e. fusion zone (FZ) and HAZ of weld using a gun drill. The diameter of the hole was measured using air probe at a different heights and orientations. These data worked as a reference for deformation against stress relaxation in further steps. A ring of inner and outer diameters of 12 and 16 mm was coaxially trepanned on electro-discharge machine (EDM), around the hole assuming it as the centreline. The hole diameter was again measured at the same heights and orientations after the trepanning process. Hence, Eq. (2) represents diametral change, where $d'(\alpha)$ and $d(\alpha)$ represent the diameter after and before the trepanning.

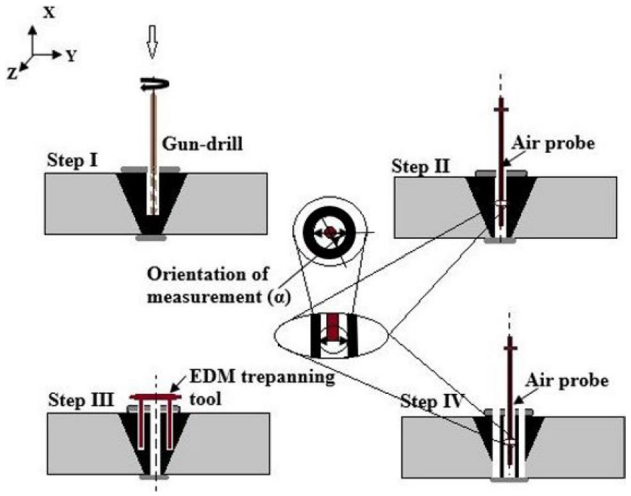

Fig. 1 Schematic of steps involved in DHD measurement

$$\Delta d\alpha = d'(\alpha) - d(\alpha) \tag{2}$$

The diametral change leads to strain calculation in different orientations for each depth throughout the thickness as given by Eqs. (3) and (4).

$$\begin{aligned}\varepsilon_{\alpha,y} = \frac{\Delta d(\alpha)}{d(\alpha)} = -\frac{1}{E}\big[&\sigma_{xx}(1+\cos 2\alpha)\\ &+\sigma_{zz}(1-\cos 2\alpha)\\ &+\tau_{xz}(4Sin2\alpha) - \upsilon\sigma_{yy}\big]\end{aligned} \tag{3}$$

$$\varepsilon_{yy} = \frac{1}{E}\left[-\sigma_{yy} - \upsilon(\sigma_{xx} + \sigma_{zz})\right] \tag{4}$$

where $\varepsilon_{\alpha,y}$ is the strain in each measurement directions of 'α' at each depth 'y' and ε_{yy} is the strain at depth 'y' in the vertical direction. σ_{ij} represent various components of stress in rectangular coordinates. The above-mentioned constitutive relation can also be written in matrix form by Eq. (5) [23].

$$\overline{\varepsilon} = -[M] \cdot \overline{\sigma} \tag{5}$$

where $\overline{\varepsilon}$ = strain vector, $[M]$ = stiffness matrix and $\overline{\sigma}$ = stress vector.

Finally, Eq. (6) gives the stress vectors as follows:

Table 2 Welding parameters for single- and double-side submerged arc welding

Parameters	Wire feed rate (mm/min)	Welding voltage (V)	Travel speed (mm/s)	Welding current (I)	Electrode stick out (mm)
Single side	200	23	5.14	560	25
Double side (first pass)	200	22.5	5.1	470	25
Double side (second pass)	200	24	5	460	25

$$\overline{\sigma} = -[M]^* \cdot \overline{\varepsilon} \tag{6}$$

where $[M]^* = ([M]^T[M])^{-1}[M]^T$.

Similarly, contour technique was also performed for longitudinal stress distribution. The contour technique is accomplished in four major steps [24]. The first step involves smooth cutting of the weld sample across the weld centreline in the transverse direction. The wire electrical discharge machine (EDM) cutting parameters to cut the sample at the mid-portion are given in Table 3. In the second step, the cut surfaces in both the cut halves were precisely measured for surface deformation against released stress. The deformation at a point defines the vertical position. The x and y coordinates on the cut surface define the location of targeted points (total number of points = 900), while z coordinate stands for vertical deformation. Hence, the probe (2-mm spherical ruby stylus) of coordinate measuring machine (CMM) (Make: Zeiss) measured the deformation with every stroke at each individual point. The placement of cut surface sample on CMM bed is sensitive for deformation measurement; hence, a specially designed fixture was used to hold the sample. The accuracy of the deformation data depends upon various factors like positioning of sample on CMM bed, cutting precision and surface roughness and probe surface and stroke, etc. The 2D plot of average surface deformation for both the cut surfaces before and after the data conditioning is shown in Fig. 2. The final and fourth step includes finite element structural modelling of surface deformation as nodal deformation load on the cut surface. Zero displacement loads were applied on the corner nodes of the weld plate model so that it can prevent its rigid body motion. The FE model of the sample with meshing and boundary conditions is shown in Fig. 3a. The best surface fitting polynomial of the surface deformation pattern was obtained to effectively apply the deformation nodal load throughout the surface. The best fitted surface plot is also shown in Fig. 3b. The negative value of deformation was applied on the nodes to generate the similar stress distribution as residual stress.

Table 3 Wire EDM cutting parameters

Parameters	Wire diameter (mm)	Wire material	Frequency (Hz)	Current (A)	Voltage (V)
Values	0.35	Brass	30–50	8–10	40–45

Mechanical Testing

Hardness and strength testing were mainly performed for comparable study of both the joints. Vickers's micro-hardness test was performed across the weld in different zones (FZ, HAZ and base metal) with a load of 2 kg and a dwell period of 10 s. ASTM E8-04 standard flat tensile specimen with 60 mm of gauge length was prepared, without removing the weld bead top and bottom reinforcement. Tensile test was conducted at room temperature at a strain rate of 0.1 mm/s. Test samples were polished with different grades of emery paper varying from coarse to fine size. The exposed surface was etched in the solution of Villella's reagent (100 ml ethanol + 2–3 g picric acid + 4–5 ml hydrochloric acid) [18, 25]. Fractography analysis was

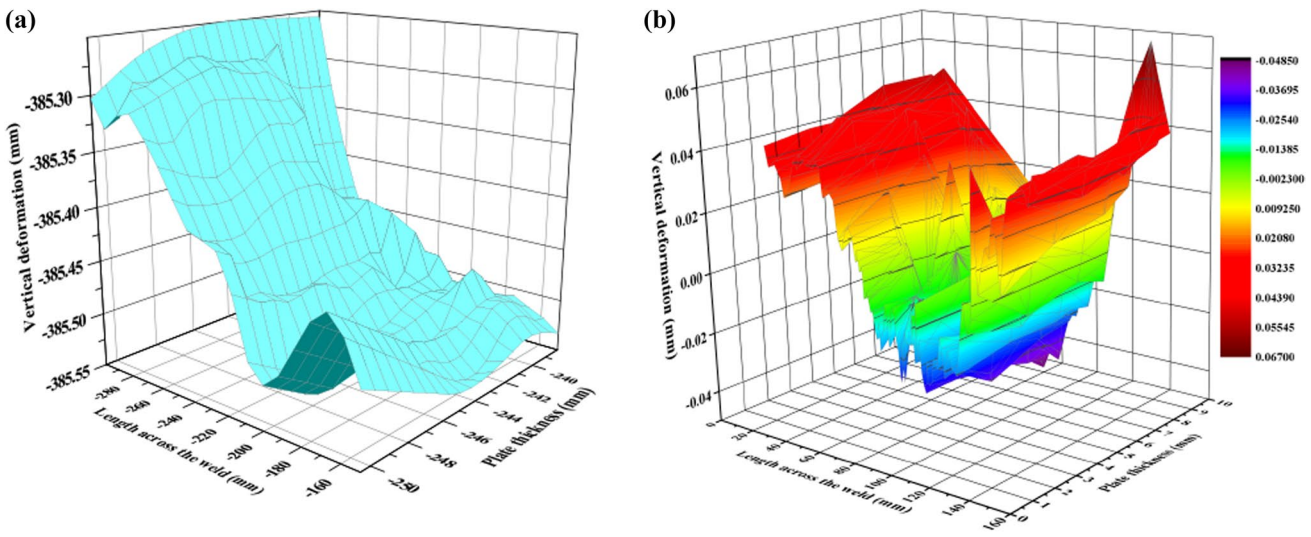

Fig. 2 Surface plot for average surface deformation of both the cut surfaces **a** before the data conditioning and **b** after the data conditioning

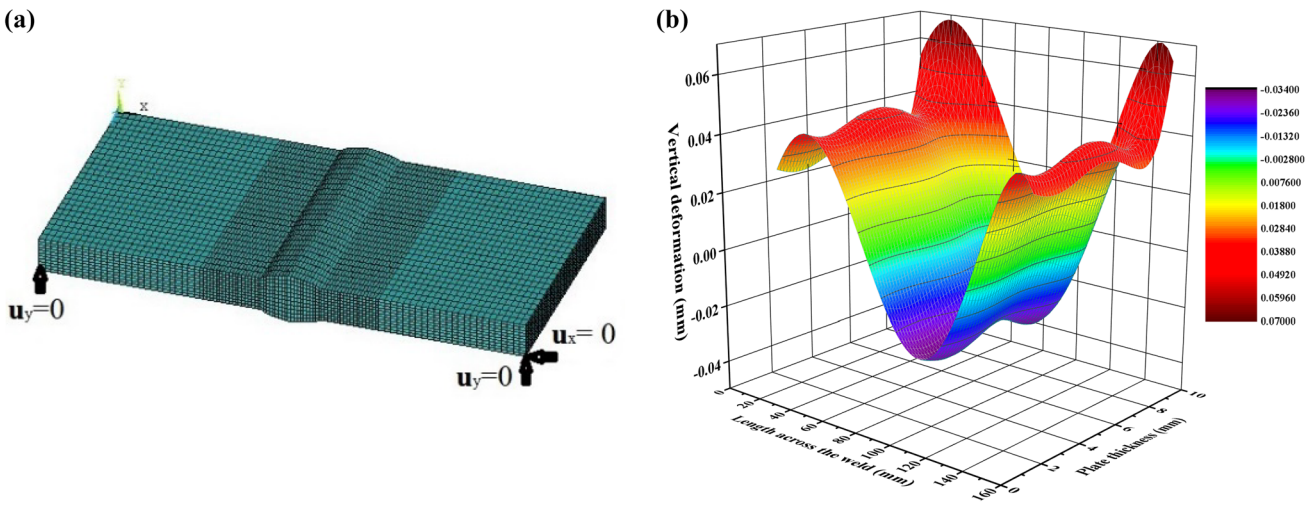

Fig. 3 **a** FE model of sample half for deformation load application and **b** best fitting surface deformation plot (Adj. R^2 value = 0.9105)

also performed using field emission scanning electron microscopy (FESEM) images for the fracture surfaces.

Finite Element Modelling

The actual single- and double-side submerged arc welding was successfully replicated using finite element modelling based on appropriate heat source model, element birth and death, temperature-dependent material properties and boundary conditions similar to the experiment. The welding simulation was carried out in two major stages of uncoupled thermal and structural analysis using ANSYS Parametric Design Language (APDL) in ANSYS Mechanical FE solver. In the present case, importance was also given on implementing the effect of austenite–martensite transformation phenomenon, associated changes in yield strength, transformation plasticity effect, etc. In thermal analysis, the actual amount of heat input was applied at the same rate of welding speed using element level heat generation for modelling inclusion of molten metal. The thermal analysis results in terms of nodal temperature are applied as the initial load on respective nodes for structural analysis considering relevant boundary conditions.

Modelling and Meshing

Both single- and double-sided SAW-welded square butt joint models are shown in Fig. 4. The mesh sensitivity was also assessed based on the convergence criterion, computing time and memory data. The smaller element size was preferred in and near the fusion zone so that the peak load in terms of heating flux or heat generation can be precisely detected. The size of the element was gradually increased for coarser size in

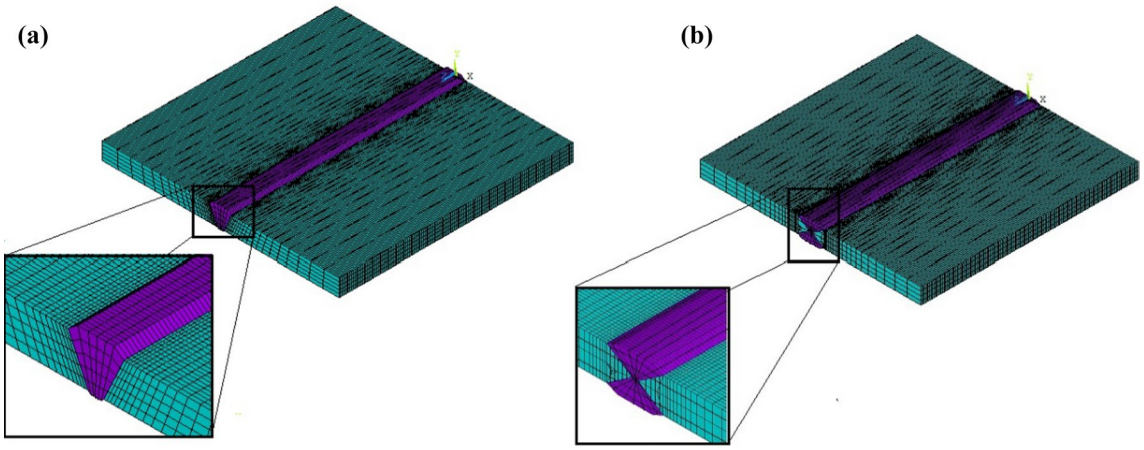

Fig. 4 Draft model and meshing of **a** single-sided single-pass weld joint, **b** double-sided single-pass weld joint

the region away from the weld centreline. One of the prime criteria for optimized meshing was the convergence value, i.e. once it reached the order of (10^{-4}) along with the good accurate results the meshing assumed as optimized. In the meshing attributes, the base metal and weld material properties were assigned to both the sections separately as differentiated with colours in Fig. 4.

Thermal Load and Heat Source Model

In the thermal modelling stage, the amount of heat input, rate of moving heat source, volume consideration of element generating heat per unit volume per unit time, etc., play an important role in the temperature distribution results. The thermal modelling also considered various assumptions and boundary conditions related to medium of heat transfer (conduction, convection or radiation), ambient condition, etc. Heat conduction model was considered for welding heat application through the element level volumetric heat generation. The element birth and death technique were applied to simulate inclusion of molten weld material in welding process. It initiates with deactivation of elements of the weld bead portion (as shown in Fig. 4) within the root gap of the weld plates. Deactivation of element signifies the multiplication of associated stiffness properties with large reduction factor which diffuses the effect of that material. Further, once the heat generation starts, the linked killed elements are reactivated with their stiffness which symbolizes the addition of new material or say welding material during the welding. A Gaussian's distributed 'volumetric double ellipsoidal heat source model' [26, 27] was adopted to model moving heat source using subroutine code written in APDL given by Eqs. (7) and (8). The convective heat transfer model was considered for cooling through heated weld plate surfaces during and after the welding. The radiation heat loss was avoided in the present case of submerged arc welding.

$$Q_{\text{front}} = \frac{6 \cdot \sqrt{3} \cdot f_{\text{front}} \cdot Q_{\text{arc}}}{a \cdot b \cdot c_{\text{front}} \cdot \pi \cdot \sqrt{\pi}} e^{\left(\frac{-3x^2}{a^2} - \frac{-3y^2}{b^2} - \frac{-3(z-vt)^2}{c_{\text{front}}^2}\right)} \tag{7}$$

$$Q_{\text{rear}} = \frac{6 \cdot \sqrt{3} \cdot f_{\text{rear}} \cdot Q_{\text{arc}}}{a \cdot b \cdot c_{\text{rear}} \cdot \pi \cdot \sqrt{\pi}} e^{\left(\frac{-3x^2}{a^2} - \frac{-3y^2}{b^2} - \frac{-3(z-vt)^2}{c_{\text{rear}}^2}\right)} \tag{8}$$

where 'Q_{front}' and 'Q_{rear}' represent the front and rear part of the heat input, v = torch travel speed, and '$\boldsymbol{a}$', '$\boldsymbol{b}$', '$\boldsymbol{c}_{\text{front}}$', '$\boldsymbol{c}_{\text{rear}}$' are the constant parameters associated with the shape and size of the weld bead of the weld joint sample. 'f_{front}' and 'f_{rear}' stand for portions of supplied heat in the front and rear part of the heat source. Its values depend on the longitudinal constant parameter, i.e., '$\boldsymbol{c}$' given by Eq. (9).

$$f_{\text{front}} = \frac{2c_{\text{rear}}}{c_{\text{front}} + c_{\text{rear}}} \;\&\; f_{\text{rear}} = \frac{2c_{\text{front}}}{c_{\text{front}} + c_{\text{rear}}}. \tag{9}$$

Material Properties and SSPT Effect

As 9Cr–1Mo–V steel belongs to the group of CSEF steels, it possesses exceptional temperature-dependent mechanical and physical properties as shown in Fig. 5. These properties must be considered in modelling. It is also recognized as a steel which experiences austenite–martensite transformation in solid state, during the heating and cooling cycles of welding. Solid-state phase transformation (SSPT) phenomenon comprises volumetric changes at microscopic level, i.e., solid-state phase changes below the solidus line. These small volumetric expansions or contractions alter the welding-induced residual stress distribution in the P91 steel weld as observed in previous literature [28, 29, 30]. Therefore, this SSPT was also considered in FE modelling. The whole SSPT occurs in two major stages, i.e., ferrite to austenite transformation during heating ($Ac_1 \le T \le Ac_3$) and austenite to martensite transformation during cooling ($M_s \le T \le M_f$). In austenitic transformation, ferrite (α) with BCC (body-centric cubic) structure transforms to austenite (γ) with FCC (face-centric cubic) structure, which leads to microscopic volumetric contraction. Similarly, in austenite (γ)–martensite (α^*) transformation, FCC structure transforms to BCT (body-centric tetragonal) structure causing volumetric expansion.

The fractional volume changes in both cases correlated with the additional strain components for phase transformation effect. The expressions in Eqs. (10–11) describe the temperature-dependent volumetric strain.

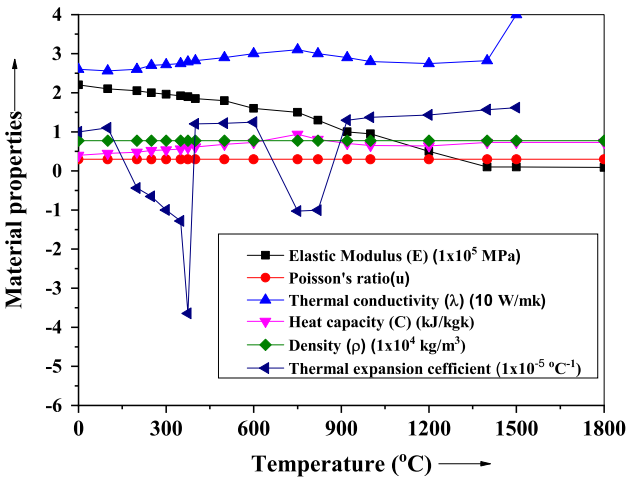

Fig. 5 Material properties for base and weld material

$$\Delta\varepsilon_{\text{vol}}\big|_{\text{Austenitic}} = \left[\frac{-2.288\times10^{-3}}{Ac_3 - Ac_1}\right]\Delta T \quad (Ac_3 \le T \le Ac_1) \tag{10}$$

$$\Delta\varepsilon_{\text{vol}}\big|_{\text{Martensitic}} = \left[3.75\times10^{-3}\left(-0.011\exp\left(-0.011(M_s - T)\right)\right)\right]\Delta T \quad (M_f \le T \le M_s) \tag{11}$$

where $\Delta\varepsilon_{\text{vol}}$ represents the volumetric strain component for both the solid-state transformation cases. In general, the values of Ac_1, Ac_3, M_s, and M_f for P91 steel are (810–20 °C), (920–30 °C), (375–80 °C) and (210–200 °C), respectively [29-32]. If the strain expression in Eqs. (10–11) is compared with the thermal strain components, the expressions in Eqs. (12–13) determine modified equivalent thermal dilation coefficient to consider the SSPT effect, also shown in Fig. 5.

$$\alpha_{\text{austenitic}} = \frac{-2.288\times10^{-3}}{Ac_3 - Ac_1} \tag{12}$$

$$\alpha_{\text{martensitic}} = 3.75\times10^{-3}\left\{-0.011\exp\left(-0.011(M_s - T)\right)\right\} \tag{13}$$

The enthalpy values for different stages of phase changes in both base and weld materials were also determined including the solid-state phase change anomaly. The temperature ranges considered for enthalpy calculation were solid-state phase transformation, mushy zone and solid–liquid phase transformations as given by Eqs. (14–18).

$$H = \rho\cdot C^*\cdot\left[T - T_{\text{o}}\right],\ \text{below solidus temperature} \tag{14}$$

where

$$C^* = C_{\text{avg}} + {}^{L}/_{(T_{\text{L}} - T_{\text{s}})}$$

$$C_{\text{avg}} = {}^{C_{\text{s}} + C_{\text{L}}}/_{2}$$

C_{s}, C_{L} and C^* represent the heat capacity at solidus temperature, liquidus temperature and specific heat of transition state, L = latent heat, T_{s} = solidus temperature, T_{L} = liquidus temperature, T = temperature below T_{s} and T_{o} = ambient temperature.

$$H_{\text{TR}} = H_{\text{s}} + \rho\cdot C\cdot\left[T_{\text{s}} - T_{\text{o}}\right],\ \text{at solidus temperature} \tag{15}$$

$$H_{\text{TR}} = H_{\text{s}} + \rho\cdot C\cdot\left[T_{\text{s}} - T_{\text{o}}\right],\ \text{at solidus}-\text{liquidus temperature} \tag{16}$$

$$H_{\text{L}} = H_{\text{s}} + \rho\cdot C^*\cdot\left[T_{\text{L}} - T_{\text{s}}\right],\ \text{at liquidus temperature} \tag{17}$$

$$H_{\infty} = H_{\text{L}} + \rho\cdot C_{\text{L}}\cdot\left[T - T_{\text{L}}\right],\ \text{above liquidus temperature.} \tag{18}$$

Structural Modelling

The welding process experiences rapid heating and cooling cycles under a constrained region which induces plastic deformation. Hence, boundary conditions, yield criterion, flow rule and hardening rule, etc., significantly affect the overall stage of combined elastic–plastic deformation in the computational modelling. Rate independent plasticity with Von Mises yield criterion was assumed considering material type (metal) and cause of deformation (welding process). Similarly, bilinear isotropic hardening model with associative flow rule was adopted for the present case. The zero-displacement load was applied on the corner nodes of the joint model in such a manner which can prevent the rigid body motion of the welding plate model. In the literatures, it is observed that tacking weld has good influence on the post-welding-induced shrinkage and angular distortion. However, it is also observed that for small sample size, the tack welds are mostly on start and end position of the weld length; as a result, it has minor effect on overall residual stress distribution in quasi-static weld region [33–36]. Hence, the effect of tacking weld may be ignored during FE modelling of submerged arc welded P91 steel plate, if the study is more focused towards quasi-static weld region.

The effect of the SSPT phenomenon was also considered in structural FE modelling. It has been observed that SSPT-induced microstructural changes also affect the yield strength of the material. Hence, the yield strength values were modified accordingly to accommodate the SSPT effect in computation modelling. The yield strength (YS) of the base material was considered for both the materials in the austenitic transformation temperature range during heating. Similarly, the YS of the weld material was taken for both the materials in the martensitic transformation temperature range during cooling. The YS and hardening modulus of the base plate and weld materials are shown in Fig. 6.

The transformation plasticity effect was also incorporated in finite element modelling by adding a negative mechanical strength factor of 30 MPa in the yield strength values of the base and weld materials in the transformation temperature range assuming it causes an equivalent effect on stress and strain developed [28].

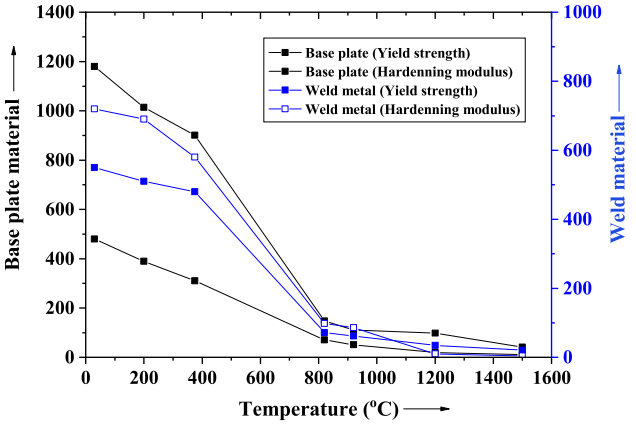

Fig. 6 YS and hardening modulus of base plate and weld material

Result and Discussion

Macro- and Micrograph

The macrographs of both single- and double-side submerged arc welded samples are shown in Fig. 7. The average width of HAZ in single-sided weld was about 7.7 mm which is reduced to around ~ 5 mm for double-pass double side welding owing to less amount of heat input per pass in double-side welding. Though, the weld bead width is almost the same for both the weld cases. A good bottom reinforcement and a decent bottom weld bead shape in single-side and double-side square butt joints are also observed from Fig. 7. The optical micrograph of as-received P91 steel plate and as-welded cases are shown in Fig. 8a. The presence of intergranular coarse and fine precipitates confirms the presence of carbides of Mo, V, Fe, etc. The tempered martensite structure with diverse prior austenite grain boundaries (PAGBs) is also observed in the microstructure of base metal. The untempered martensite structure is observed in the fusion zone of all the three as-welded cases. The amount of **δ** Ferrite in the microstructure distinguishes the welding cases. The high heat input of 2.3 kJ/mm in single-side single-pass submerged arc welding is characterized by large patches of **δ** Ferrite present in the fusion zone [37]. As expected, the microstructure of FZ of second pass region of double-sided weld consists of comparatively smaller patches of **δ** Ferrite subjected to lower heat input of 1.8–1.9 kJ/mm, whereas less number of ferrite patches is observed in first-pass weld. It signifies that second weld pass works as post-weld heating process which leads to auto-tempering and transforms the δ-ferrite to austenite structure. A negative effect of **δ** ferrite on mechanical properties of P91 steel weldments has been observed [38, 39].

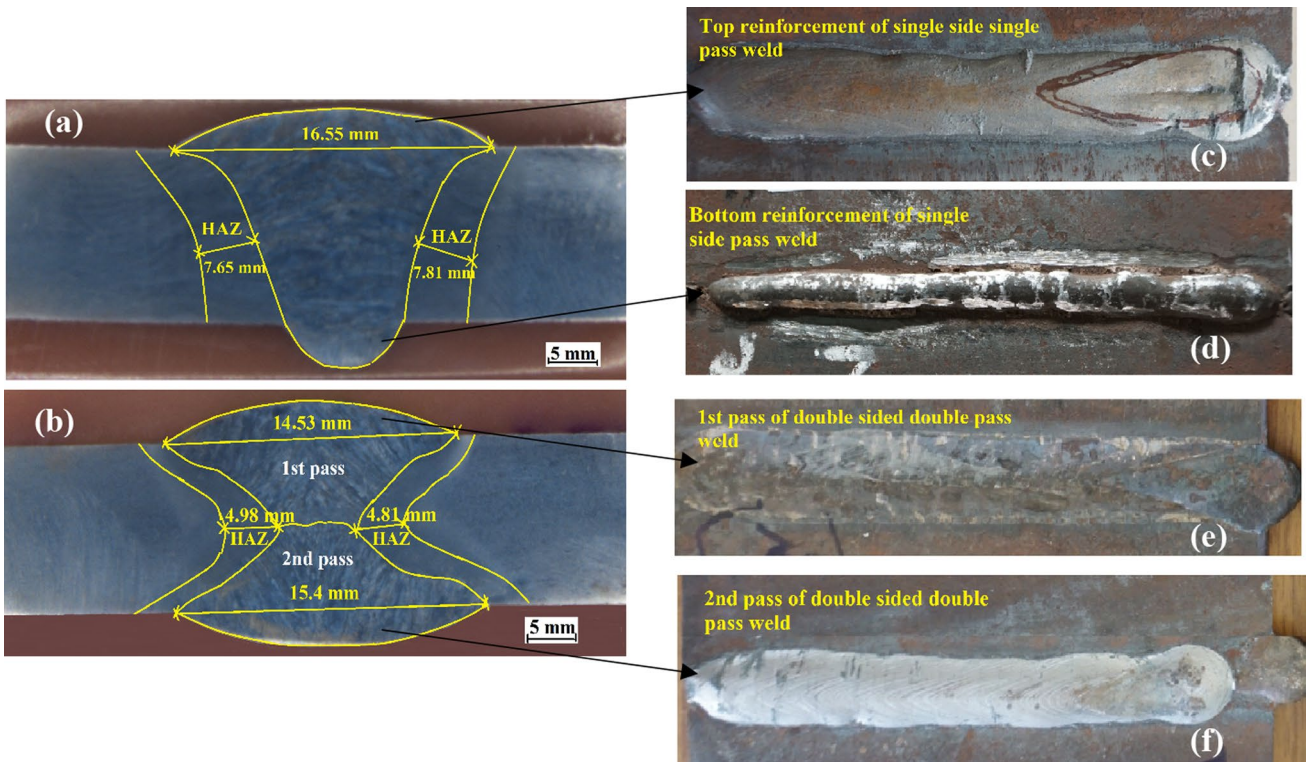

Fig. 7 Macrograph of **a** single- and **b** double-side single-pass welded samples, **c** top and **d** bottom reinforcement in single-side single-pass weld, weld bead of **e** first- and **f** second-pass welds in double-sided double-pass weld sample

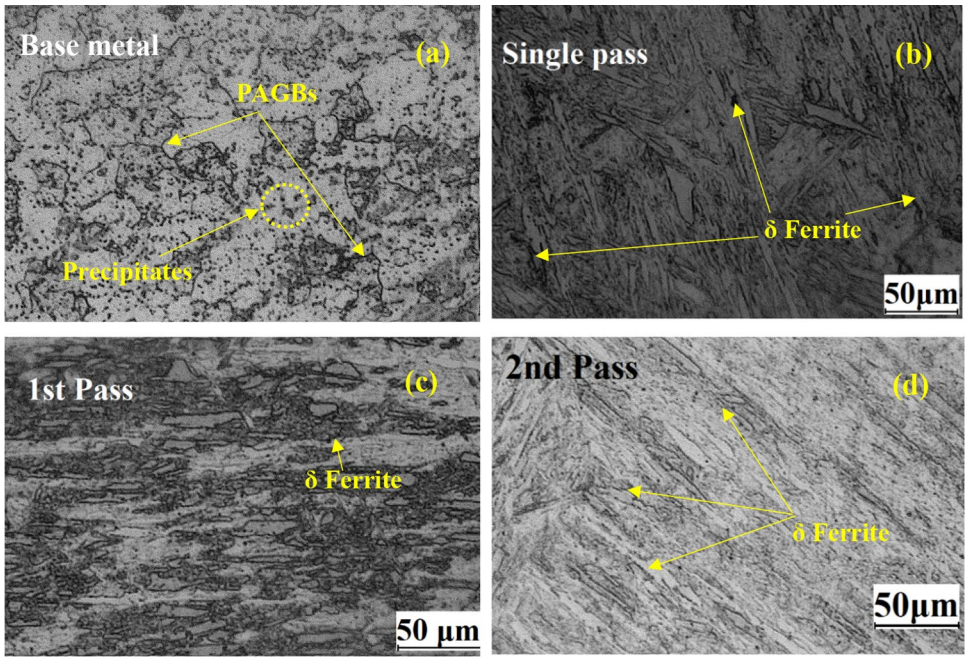

Fig. 8 Microstructure of weld fusion zone **a** base metal, **b** single-side single-pass weld, **c** first pass of double-sided weld and **d** second pass of double-sided weld

Temperature Distribution

The time-dependent thermal profile and temperature gradient for single-sided and double-sided welded joints are shown in Fig. 9. The thermal profile for single-side welded sample shows the peak temperature as around 389 °C for a point at a distance of 15 mm away from the weld centreline, whereas for double-sided weld the peak temperature is observed to be 547 °C for the first weld pass at point 10 mm away from the weld centreline. Similarly, the peak temperature for second pass on the bottom side of the plate is about 610 °C at a distance of 12 mm away from the weld centreline. The contribution of previous weld pass to the peak temperature in second weld pass is clearly observed. The temperature contour plots for both single- and double = side welds reveal FZ, HAZ and base metal sections based on the temperature distribution colour bands. The predicted thermal profile for both the weld types fairly matched the experimentally recorded temperature plot. Similarly, the macrographs of welded joints were also adequately replicated with the predicted temperature contours. It is observed that for single side weld, the peak temperature range for molten metal zone (1882.4–1470 °C) is higher than the same temperature ranges of first (1700–1513 °C) and 2nd (1755–1523 °C) weld passes in double side welding. These predicted temperatures as fairly match the experimental results, and it was efficiently applied as temperature load in the structural analysis.

Hardness and Mechanical Strength

The contour plots of micro-hardness values across the weld for single-sided and double-sided welds are shown in Fig. 10a, b, respectively. For single-sided weld, the average value of highest micro-hardness in the FZ is observed as 408 HV, whereas double-sided single-pass welding shows lower value of hardness distribution with an average value of 389 HV. The heating and cooling cycles stimulate the plastic deformation and work hardening effect in the weld metal [40]. Hence, high heat input and fast cooling rate in single-sided welding result in higher hardness value. Maduraimuthu et al. also observed similar kind of hardness difference between activated-TIG (single-pass) and double-pass TIG welded P91 steel weld [41]. However, the hardness values in the HAZ were found almost the same for both the cases. As far as strength is concerned, the stress–strain plots for single- and double-side welded samples and base metal are collectively shown in Fig. 11. The tensile properties of these cases are also enlisted in Table 4.

Single-side weld exhibits high tensile strength of 615 MPa compared to 574 MPa of tensile strength of double-sided weld joints which is expectedly higher than the base metal strength (581 MPa). The higher strength of single-sided weld joint indicates the presence of hardened martensite structure from high cooling rate, while the tempering of martensite in double-pass welding contributes to less strength.

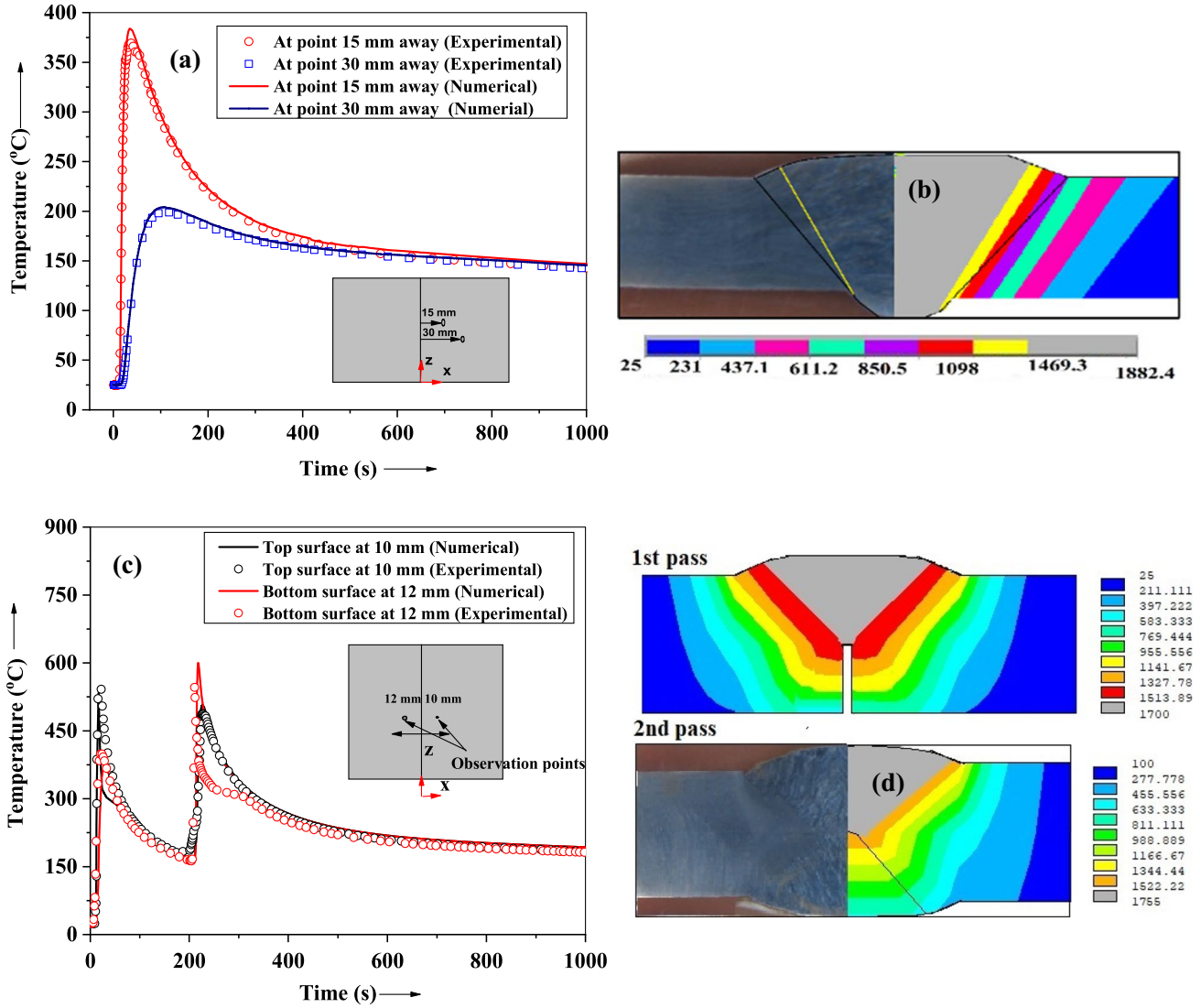

Fig. 9 Thermal profile and temperature contour for **a**, **b** single-side single-pass and **c**, **d** double-side single-pass weld, respectively

Though the fracture occurring in the base metal region explains the normalized and tempered martensite condition in it, the higher strength of weld joints also relates to the lower % elongation values in both the weld cases compared to the base metal. The cone-shaped cross section of the fracture surface as shown in Fig. 12a, exposes the ductile fracture in the weld. Similarly, the presence of adequate number of dimples, voids, tear ridge and cleavage facets prove the ductile nature of failure in tensile test of base metal and weld joint samples as shown in Fig. 12b–d.

Residual Stress

Figure 13 presents the longitudinal residual stress distribution across the thickness of the FZ of single- and double-sided welds. A compressive residual stress was observed in the FZ of the single-sided weld, whereas the double-sided weld reveals a tensile residual stress in the mid-thickness region of the weld fusion zone. In general, volumetric shrinkage in the weld develops a tensile residual stress during the cooling process in most of the steel weld. Nevertheless, the martensitic transformation in the P91 steel weld stirred up the microscopic volumetric expansion unlike other steels. Beside high amount of heat input, single-side single-pass welding also involves comparatively lesser amount of weld material and also experienced high cooling rate. The lesser volume of weld metal causes lesser volumetric shrinkage effect (i.e., less tensile residual stress), while high rate of cooling leads to more martensitic transformation-induced volumetric expansion effect, which collectively established a compressive residual stress in the single-sided weld joint. On the other hand, relatively high volume of weld metal and

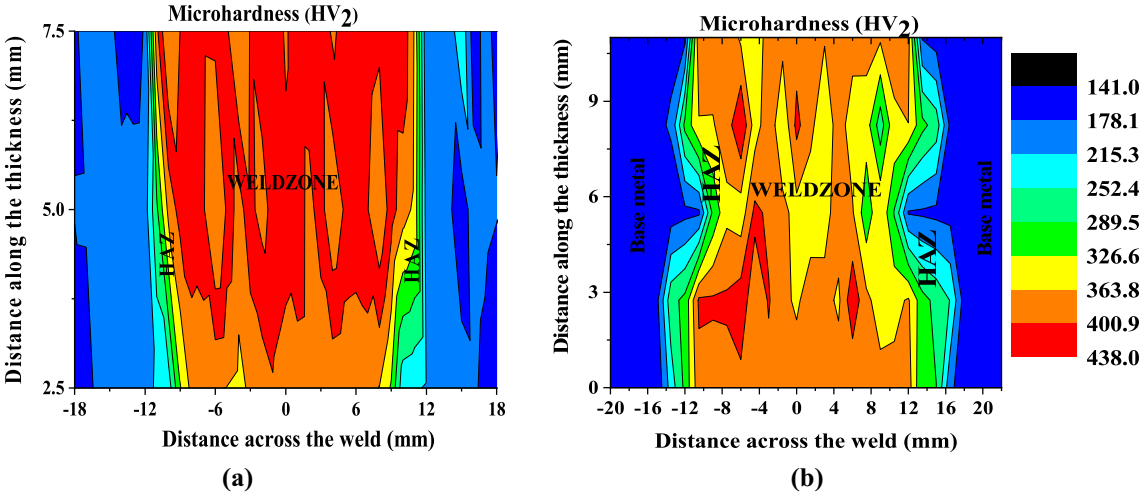

Fig. 10 Contour plot of micro-hardness value in **a** single-sided weld, **b** double-sided weld

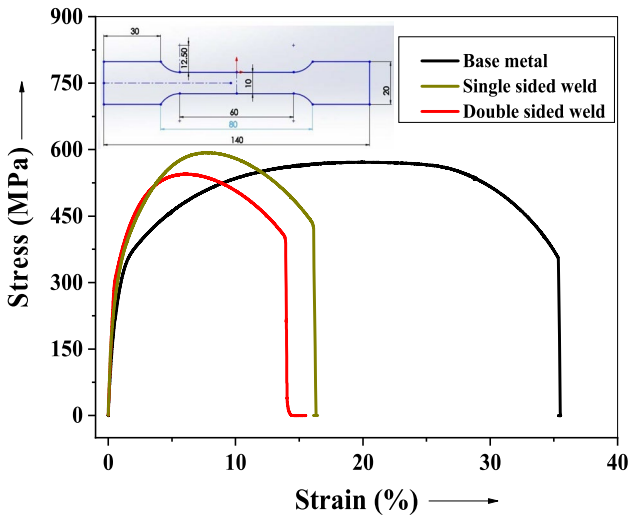

Fig. 11 Engineering stress versus engineering strain curve at room temperature

slower cooling rate (especially in the mid-thickness region) of the double-sided weld shaped up a tensile residual stress on the same ground mentioned for single-sided weld. However, the top and bottom sections of the double-sided weld possess more exposed areas for a better rate of cooling. It stimulated an additional martensitic transformation and resulted in volumetric expansion during cooling. Hence, a compressive residual stress was observed in these sections which is also shown in Fig. 13. A similar compressive or low tensile residual stress pattern throughout the thickness of FZ has been observed for laser-welded square butt single-pass joint of 10-mm-thick grade 91 steel [42].

The finite element modelling was performed for both the weld models for better understanding of residual stress distribution considering the limitation of DHD and contour techniques. The finite element predicted results can allow access to explore the status of residual stresses in both across the weld centreline and across the thickness throughout the weld plate region. Figure 14 presents the contour plot of longitudinal residual stress distribution across the thickness of the plate. The mid-section (similar to contour technique) of double-sided weld and a section parallel to the hole (similar to DHD technique) in the single-sided weld were considered for the contour plot. The predicted results exhibit the comparable longitudinal residual stress in both the weld cases. In double-sided weld, the top and bottom sections possess compressive residual stress equivalent to experiment results. Similarly, single-sided weld shows compressive longitudinal stress in the FZ throughout the thickness of the weld. Hence, the predicted results fairly matched with the experimental one with minimum prediction error of 3.15% and 4.2% for single- and double-sided welds, respectively.

Table 4 Tensile properties of base metal, single- and double-sided welds

Sl. no.	Sample	Tensile strength (MPa)	0.2% offset yield strength (MPa)	% Elongation	Fracture location
1	Single side	615	513	16.5	Base plate
2	Double side	574	318	14.8	Base plate
3	Base metal	581	314	35.6	–

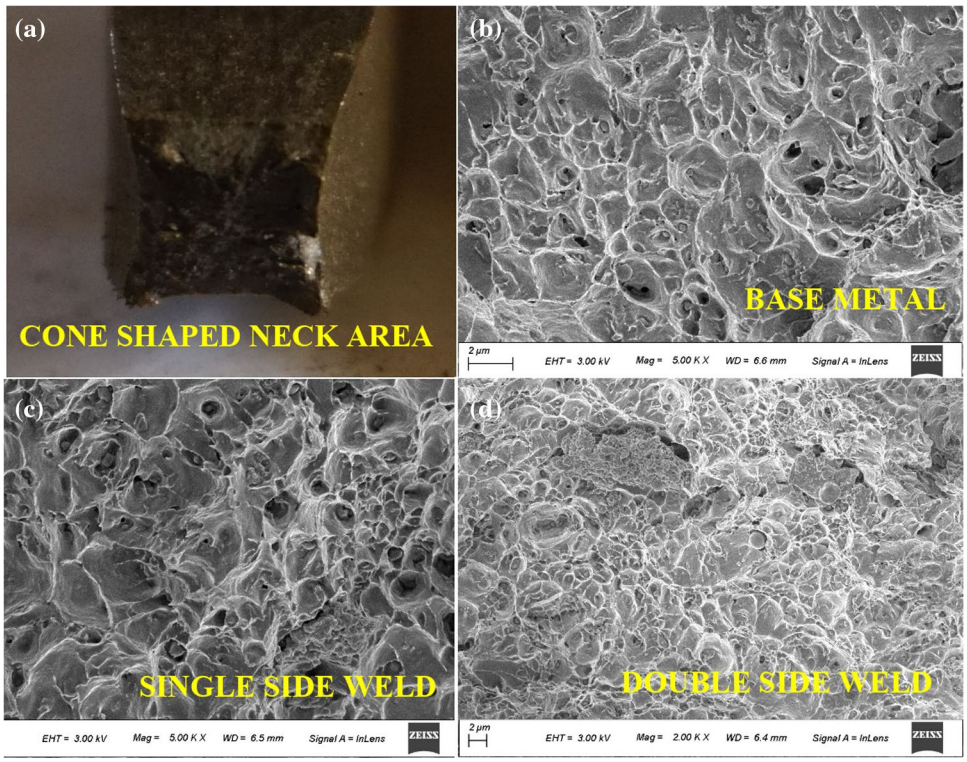

Fig. 12 **a** Cross section of one of the fracture surfaces (base metal), SEM fractography images of **b** base metal, **c** single-side weld, **d** double-side weld

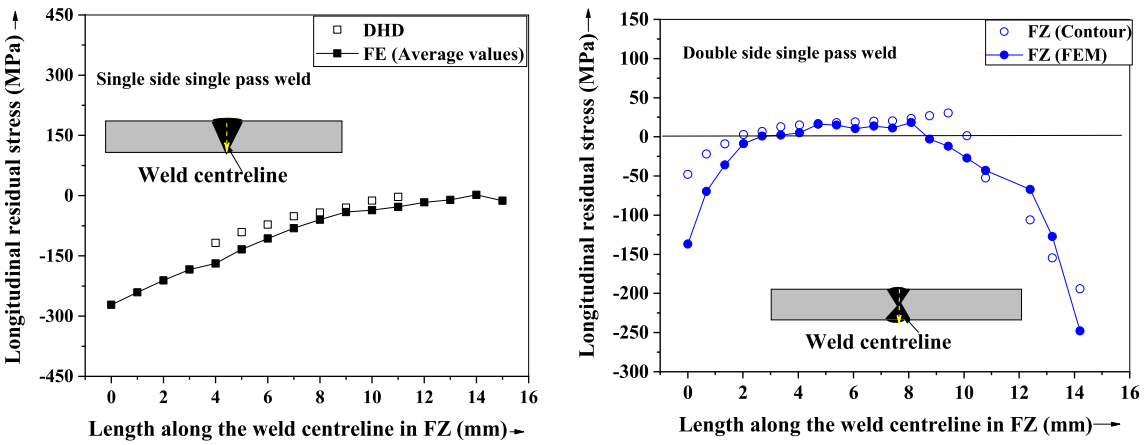

Fig. 13 Longitudinal residual stress in the fusion zone of submerged arc single- and double-side single-pass square butt weld joints of P91 steel

Conclusions

Single- and double-side single-pass submerged arc welding was carried out on a P91 steel plate. An experimental and finite element investigation was performed for comparative study of residual stress, mechanical properties and microstructural evolution, etc. On the basis of studies performed, the following conclusions can be made:

1. A good depth of penetration was achieved with single-side single-pass submerged arc welding of 10-mm-thick P91 steel butt joint, without any edge preparation.
2. Single-sided weld exhibited higher hardness value, transverse yield and ultimate strength as compared to double-sided weld joint. The ductility was observed almost similar for both the weld cases.
3. A compressive residual stress was observed throughout the thickness of the single-sided weld, while the double-

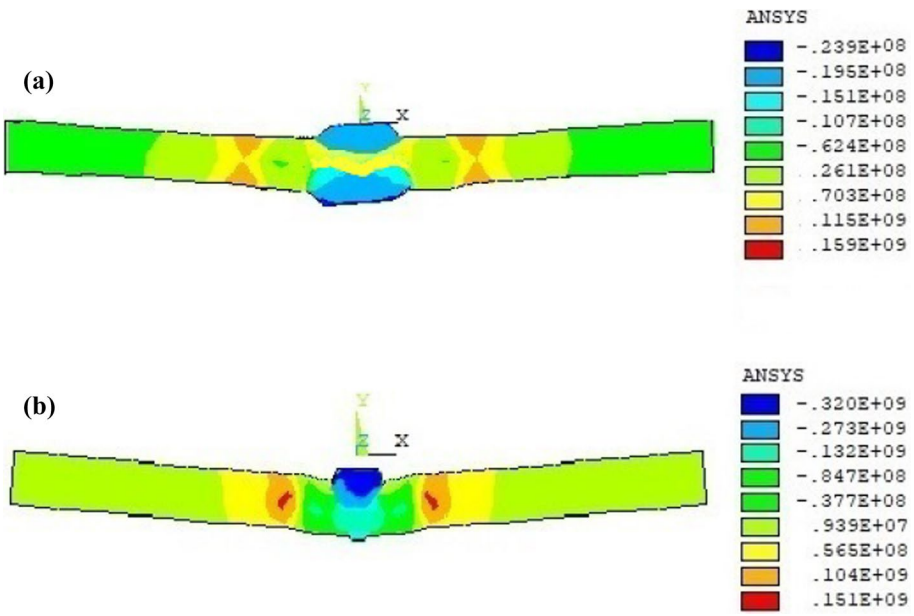

Fig. 14 Contour of longitudinal residual stress across the weld plate thickness in **a** double-sided weld (mid-section), **b** single-sided weld (section parallel to DHD measurement location)

sided weld exhibited tensile residual stress in the mid-thickness region.

4. The high heat input and faster cooling rate in single-side single-pass welding contributed to coarser microstructure, large patches of **δ** ferrite and notable martensitic transformation, respectively.
5. The overall effect of solid-state phase transformation was efficaciously implemented in FE modelling and simulation of the joint using ANSYS Parametric Design Language.
6. The FE predicted results fairly matched with the experiment with a prediction error of 3.15% and 4.2% for single- and double-sided welding, respectively.

Funding There were no funds received to accomplish this work.

Declarations

Conflict of interest The authors hereby assure that there are no competing financial interests or personal relationships that could affect the work described in this paper.

References

1. C. Pandey, A. Giri, M.M. Mahapatra, Evolution of phases in P91 steel in various heat treatment conditions and their effect on microstructure stability and mechanical properties. Mater. Sci. Eng. A **664**, 58–74 (2016). https://doi.org/10.1016/j.msea.2016.03.132
2. C. Pandey, M.M. Mahapatra, P. Kumar, N. Saini, A. Srivastava, Microstructure and mechanical property relationship for different heat treatment and hydrogen level in multi-pass welded P91 steel joint. J. Manuf. Process. **28**, 220–234 (2017). https://doi.org/10.1016/j.jmapro.2017.06.009
3. S. Suman, P.V.S.S. Sridhar, P. Biswas, D. Das, Prediction of welding-induced distortions in large weld structure through improved equivalent load method based on average plastic strains. Weld. World **64**(1), 179–200 (2020). https://doi.org/10.1007/s40194-019-00805-1
4. D. Akbari, I. Sattari-Far, Effect of the welding heat input on residual stresses in butt-welds of dissimilar pipe joints. Int. J. Press. Vessels Pip. **86**(11), 769–776 (2009). https://doi.org/10.1016/j.ijpvp.2009.07.005
5. R. Gadallah, N. Osawa, S. Tanaka, S. Tsutsumi, Critical investigation on the influence of welding heat input and welding residual stress on stress intensity factor and fatigue crack propagation. Eng. Fail. Anal. **89**, 200–221 (2018). https://doi.org/10.1016/j.engfailanal.2018.02.028
6. A. Ravisankar, S.K. Velaga, G. Rajput, S. Venugopal, Influence of welding speed and power on residual stress during gas tungsten arc welding (GTAW) of thin sections with constant heat input: a study using numerical simulation and experimental validation. J. Manuf. Process. **16**(2), 200–211 (2014). https://doi.org/10.1016/j.jmapro.2013.11.002
7. A. Ishigami, M.J. Roy, J.N. Walsh, P.J. Withers, The effect of the weld fusion zone shape on residual stress in submerged arc welding. Int. J. Adv. Manuf. Technol. **90**(9–12), 3451–3464 (2017). https://doi.org/10.1007/s00170-016-9542-z
8. H. Vemanaboina, B. Sridhar Babu, E. Gundabattini, P. Ferro, K. Kumar, Effect of heat input on distortions and residual stresses induced by gas tungsten arc welding in SS 316L to INCONEL625 multipass dissimilar welded joints. Adv. Mater. Sci. Eng. **2021**, 1–9 (2021). https://doi.org/10.1155/2021/1028461
9. A.R. Kohandehghan, S. Serajzadeh, Arc welding induced residual stress in butt-joints of thin plates under constraints. J. Manuf. Process. **13**(2), 96–103 (2011). https://doi.org/10.1016/j.jmapro.2011.01.002
10. G. Fu, M.I. Lourenco, M. Duan, S.F. Estefen, Effect of boundary conditions on residual stress and distortion in T-joint welds 3D finite element model a B. JCSR **102**, 121–135 (2014). https://doi.org/10.1016/j.jcsr.2014.07.008

11. M. Kartal, M. Turski et al., Residual stress measurements in single and multi-pass groove weld specimens using neutron diffraction and the contour method. Mater. Sci. Forum **524–525**, 671–676 (2006). https://doi.org/10.4028/www.scientific.net/msf.524-525.671
12. M. Hashemzadeh, B.Q. Chen, C. Guedes-Soares, Evaluation of multi-pass welding-induced residual stress using numerical and experimental approaches. Ships Offshore Struct. **13**(8), 847–856 (2018). https://doi.org/10.1080/17445302.2018.1470453
13. A.K. Mondal, P. Biswas, S. Bag, Experimental and FE analysis of submerged arc weld induced residual stress and angular deformation of single and double sided fillet welded joint. Int. J. Steel Struct. **17**(1), 9–18 (2017). https://doi.org/10.1007/s13296-016-0093-9
14. I. Sattari-Far, M.R. Farahani, Effect of the weld groove shape and pass number on residual stresses in butt-welded pipes. Int. J. Press. Vessels Pip. **86**(11), 723–731 (2009). https://doi.org/10.1016/j.ijpvp.2009.07.007
15. M. Venkatesh Kannan, N. Arivazhagan, M. Nageswara Rao, G. Madhusudhan Reddy, K.V. Phani Prabhakar, P. Gadhe, Studies on microstructure and mechanical properties of weldments produced in 12 Mm thick naval grade high strength low alloy steel for sub-zero application by single and double pass hybrid laser arc welding. J. Mater. Eng. Perform. (2021). https://doi.org/10.1007/s11665-021-06403-x
16. C. Pandey, M.M. Mahapatra, P. Kumar, A comparative study of transverse shrinkage stresses and residual stresses in P91 welded pipe including plasticity error. Arch. Civ. Mech. Eng. **18**(3), 1000–1011 (2018). https://doi.org/10.1016/j.acme.2018.02.007
17. S. Suman, P. Biswas, Thermo-mechanical study of single and multi-pass welding of CSEF steel for residual stresses and deformations considering solid state phase transformation. Mater. Today Proc. **28**, 789–795 (2020). https://doi.org/10.1016/j.matpr.2019.12.299
18. S. Suman, P. Biswas, A. Tiwari, Microstructure evolution and mechanical behaviour of SAW weldments of CSEF steel on preheating and PWHT. Trans. of Indian Institute Metals, 73, 1185-1197, (2020). https://doi.org/10.1007/s12666-020-01961-5
19. S. Suman, A. Tiwari, P. Biswas, M.M. Mahapatra, Finite element analysis of thermal-induced stresses in submerged arc welded chromium-molybdenum steel and their mitigation through heat treatment. J. Mater. Eng. Perform. **29**(12), 8271–8285 (2020). https://doi.org/10.1007/s11665-020-05262-2
20. S. Suman, P. Biswas, Computational modelling of in-process mitigation technique to control residual stress in thick plate welding,next generation materials and processing technologies, Vol 9. Springer Proceedings in Materials, Springer, Singapore, pp 333-341 (2021). https://doi.org/10.1007/978-981-16-0182-8_25
21. S. Suman, P. Biswas, Comparative study on SAW welding induced distortion and residual stresses of CSEF steel considering solid state phase transformation and preheating. J. Manuf. Process. **51**, 19–30 (2020). https://doi.org/10.1016/j.jmapro.2020.01.012
22. N.R. Mandal, R. Maiti, Study of single side single pass submerged arc welding using reusable backing strip. Sci. Technol. Weld. Join. **10**(3), 319–324 (2005). https://doi.org/10.1179/174329305X40633
23. E. Kingston, D.J. Smith, G. Zheng, C. Gill, P. Hurrell, Measurement of residual stresses in thick section steel electron beam welds. Proceedings of the ASME 2010 Pressure Vessels and Piping Division/K-PVP Conference. ASME 2010 Pressure Vessels and Piping Conference: Vol. 6, Bellevue, Washington, USA. July 18–22, 2010. pp. 1307-1316. ASME. https://doi.org/10.1115/PVP2010-25314
24. S. Suman, P. Biswas, S.K. Patel, V.P. Singh, A. Kumar, B. Kuriachen, Measurement of residual stresses in submerged arc welded P91 steel using surface deformation. Mater. Today Proc. **21**, 1707–1712 (2020)
25. C. Pandey, M.M. Mahapatra, Effect of groove design and post-weld heat treatment on microstructure and mechanical properties of P91. J. Mater. Eng. Perform. **25**(7), 2761–2775 (2016). https://doi.org/10.1007/s11665-016-2127-z
26. J. Goldak, A. Chakravarti, M. Bibby, A new finite element model for welding heat sources. Metall. Trans. B **15**, 299–305 (1984). https://doi.org/10.1007/BF02667333
27. S. Suman, P. Biswas, S. Baranwal, V. Mekala, Finite element modelling of side heating for mitigation of residual stress and distortion in SAW welded P91 steel weld. Mater. Today Proc. **28**, 2511–2521 (2020)
28. A.H. Yaghi, T.H. Hyde, A.A. Becker, W. Sun, Numerical simulation of P91 pipe welding including the effects of solid-state phase transformation on residual stresses. Proc. Inst. Mech. Eng. Part L J. Mater. Des. Appl. **221**(4), 213–224 (2007). https://doi.org/10.1243/14644207JMDA152
29. A.H. Yaghi, T.H. Hyde, A.A. Becker, J.A. Williams, W. Sun, Residual stress simulation in welded sections of P91 pipes. J. Mater. Process. Technol. **167**(2–3), 480–487 (2005). https://doi.org/10.1016/j.jmatprotec.2005.05.036
30. S. Suman, P. Biswas, Finite element analysis of in-process thermal mitigation of welding induced residual stresses in 9Cr-1Mo-V steel butt joint considering phase transformation. J. Manuf. Proc. **70**, 361–375 (2021)
31. A. Kundu, P.J. Bouchard, S. Kumar, G.K. Dey, C.E. Truman, Residual stresses in P91 steel electron beam welds. Sci. Technol. Weld. Join. **18**(1), 70–75 (2013). https://doi.org/10.1179/136217181 2Y.0000000076
32. A.H. Yaghi, T.H. Hyde, A.A. Becker, W. Sun, Thermo-mechanical modelling of P91 steel weld microstructure and residual stresses in power plant pipework, in *1st Int. Conf. Sustain. Power Gener. Supply, SUPERGEN '09*, no. September, 2009. https://doi.org/10.1109/SUPERGEN.2009.5348007
33. A.K. Mondal, P. Biswas, S. Bag, Influence of tacking sequence on residual stress and distortion of single sided fillet submerged arc welded joint. J. Mar. Sci. Appl. **14**(3), 250–260 (2015). https://doi.org/10.1007/s11804-015-1320-z
34. Y. Fang, L. Li, X. Meng, J. Lv, J. Shi, Study on the influence of tack welding on residual stress of overlap joint. Iceep **143**, 769–773 (2017). https://doi.org/10.2991/iceep-17.2017.134
35. C. Heinze, C. Schwenk, M. Rethmeier, The effect of tack welding on numerically calculated welding-induced distortion. J. Mater. Process. Technol. **212**(1), 308–314 (2012). https://doi.org/10.1016/j.jmatprotec.2011.09.016
36. M. Abid, M. Siddique, Numerical simulation to study the effect of tack welds and root gap on welding deformations and residual stresses of a pipe-flange joint. Int. J. Press. Vessels Pip. **82**(11), 860–871 (2005). https://doi.org/10.1016/j.ijpvp.2005.06.008
37. K.S. Chandravathi, K. Laha, K. Bhanu Sankara Rao, S.L. Mannan, Microstructure and tensile properties of modified 9Cr–1Mo steel (Grade 91). Mater. Sci. Technol. **17**(5), 559–565 (2001). https://doi.org/10.1179/026708301101510212
38. C. Pandey, M. Mohan Mahapatra, P. Kumar, R.S. Mulik, N. Saini, J. Gopal Thakre, Effect of welding process and PWHT on δ-ferrite evolution in dissimilar P91 and P92 steel joint. Mater. Today Proc. **5**(9), 17080–17088 (2018). https://doi.org/10.1016/j.matpr.2018.04.115
39. S. Suman, P. Biswas, Finite element analysis of in-process thermal mitigation of welding induced residual stresses in 9Cr-1Mo-V steel butt joint considering phase transformation. J. Manufact. Process, **70**(1), 361–375 (2021)
40. I. Gowrisankar, A.K. Bhaduri, V. Seetharaman, D.D.N. Verma, D.R.G. Achar, Effect of the number of passes on the structure and

properties of submerged arc welds of Aisi type 316L stainless steel. Weld. J. (Miami, Fla) **66**(5), 147–154 (1987)
41. V. Maduraimuthu, M. Vasudevan, V. Muthupandi, A.K. Bhaduri, T. Jayakumar, Effect of activated flux on the microstructure, mechanical properties, and residual stresses of modified 9Cr–1Mo steel weld joint. Metall. Mater. Trans. B Process Metall. Mater. Process. Sci. **43**(1), 123–132 (2012). https://doi.org/10.1007/s11663-011-9568-4
42. S. Kumar, A. Kundu, K.A. Venkata, A. Evans, C.E. Truman, G.K. Dey, Residual stresses in laser welded ASTM A387 Grade 91 steel plates. Mater. Sci. Eng. A **575**, 160–168 (2013). https://doi.org/10.1016/j.msea.2013.03.046